

The multipolar structure of rotating boson stars

Massimo Vaglio,^{1,2} Costantino Pacilio,^{1,2} Andrea Maselli,^{3,4} and Paolo Pani^{1,2}

¹*Dipartimento di Fisica, “Sapienza” Università di Roma, Piazzale Aldo Moro 5, 00185, Roma, Italy*

²*INFN, Sezione di Roma, Piazzale Aldo Moro 2, 00185, Roma, Italy*

³*Gran Sasso Science Institute (GSSI), I-67100 L’Aquila, Italy*

⁴*INFN, Laboratori Nazionali del Gran Sasso, I-67100 Assergi, Italy*

(Dated: March 16, 2022)

The relativistic multipole moments provide a key ingredient to characterize the gravitational field around compact astrophysical objects. They play a crucial role in the description of the orbital evolution of coalescing binary systems and encode valuable information on the nature of the binary’s components, which leaves a measurable imprint in their gravitational-wave emission. We present a new study on the multipolar structure of a class of arbitrarily spinning boson stars with quartic self-interactions in the large coupling limit, where these solutions are expected to be stable. Our results strengthen and extend previous numerical analyses, showing that even for the most compact configurations the multipolar structure deviates significantly from that of a Kerr black hole. We provide accurate data for the multipole moments as functions of the object’s mass and spin, which can be directly used to construct inspiral waveform approximants and to perform parameter estimations and searches for boson star binaries.

I. INTRODUCTION

The advent of gravitational-wave (GW) astronomy has opened new opportunities for tests of fundamental physics [1]. A cornerstone of this program is to use GW data to probe the nature of compact objects [2–4], and in particular to explore the possibility that astrophysical compact sources other than black holes (BH) and neutron stars can exist in the Universe. These hypothetical objects can provide a new portal to test a variety of particle and high-energy physics models [5, 6] and could be an exotic explanation [7] for the LIGO/Virgo “mass-gap events” (e.g. GW190814 [8] and GW190521 [8, 9]) which do not fit naturally within the standard astrophysical formation scenarios for BHs and neutron stars.

Among the plethora of exotic compact objects [2], boson stars (BSs) stand out as one of the best motivated models arising from a concrete field theory. BSs are self-gravitating solitons, composed of either scalar [10–12] or vector [13], massive complex fields, minimally coupled to Einstein’s gravity (see [14, 15] for some reviews). At variance with other models, for BSs the whole dynamics (including BS mergers [7, 16–19] and nonlinear stability analysis [20–22]) and phenomenology can be studied from first principles. They are therefore a natural target for GW searches.

Deviations in the GW inspiral signals with respect to the case of BH and neutron star binaries can be traced back to the so-called finite-size effects, which encode the properties of the object’s internal structure. In a post-Newtonian expansion of Einstein’s field equations for a binary system, the leading-order effect depending on the internal structure of the binary components is the spin-induced mass quadrupole moment, M_2 [23]. According to General Relativity, if the object is a stationary BH, it must be axisymmetric and described by the Kerr solution. Due to the symmetries of the latter, the multipolar structure of a BH in General Relativity is encoded in a

closed-form, elegant, relation [24]

$$M_\ell^{\text{BH}} + iS_\ell^{\text{BH}} = M^{\ell+1} (i\chi)^\ell, \quad (1)$$

where M_ℓ (S_ℓ) are the Geroch-Hansen mass (current) multipole moments [24, 25], $M \equiv M_0$ is the mass, $J \equiv S_1$ is the angular momentum, and $\chi \equiv J/M^2$ is the dimensionless spin¹. Introducing the dimensionless quantities $\bar{M}_\ell \equiv M_\ell/M^{\ell+1}$ and $\bar{S}_\ell \equiv S_\ell/M^{\ell+1}$, the only nonvanishing moments of the Kerr spacetime are

$$\bar{M}_{2n}^{\text{BH}} = (-1)^n \chi^{2n}, \quad \bar{S}_{2n+1}^{\text{BH}} = (-1)^n \chi^{2n+1} \quad (2)$$

for $n = 0, 1, 2, \dots$. Besides the fact that the entire multipolar structure is completely determined only by the BH mass and spin, having $M_\ell = 0$ ($S_\ell = 0$) when ℓ is odd (even) is a consequence of the equatorial symmetry of the Kerr metric, whereas the fact that all nonvanishing ℓ -th multipoles (with $\ell \geq 2$) are proportional to χ^ℓ is a peculiarity of the Kerr metric.

Any deviation from the above multipolar structure would imply that the underlying spacetime is not described by the Kerr solution. Therefore, measuring any multipole moment of a compact object in addition to the mass and spin would provide a null-hypothesis tests of the Kerr metric [1, 2, 30–34].

Going beyond null-hypothesis tests (e.g. if one wishes to perform model selection between the Kerr hypothesis and a more exotic model) requires computing the multipolar structure of alternative objects. In particular, the

¹ For a generic spacetime the multipole moments of order ℓ are rank- ℓ tensors, $M_{\ell m}$ and $S_{\ell m}$, which reduce to scalar quantities, M_ℓ and S_ℓ , in the axisymmetric case, see e.g. Refs. [26, 27] for the general definitions. In this paper we shall only focus on axisymmetric and equatorial symmetric spacetimes and therefore we shall only deal with scalar quantities with the same symmetries of Kerr’s (see [28, 29] for a recent work in which the equatorial and axial symmetries are relaxed).

multipolar structure of BSs differs from that of a BH and depends on the underlying scalar self-interactions [6, 35], similarly to the case of neutron stars where the multipole moments depend on the underlying equation of state.

The multipolar structure of BSs with quartic scalar interactions was computed in a seminal paper by Ryan [35] by using a perfect-fluid approximation scheme valid in the large self-coupling regime and implementing an iterative method to solve for Einstein's equations in the stationary and axisymmetric case. The scope of this work is to extend Ryan's analysis in order to accurately compute the leading-order moments (the mass quadrupole and the current octupole) in the entire parameter space of the model, and to provide accurate data, useful to build waveform templates [36–38] for actual searches and parameter estimation. Henceforth we adopt $G = c = 1$ units.

II. THEORETICAL SETUP

We consider stationary axisymmetric BSs as solutions of the Einstein–Klein–Gordon equations for a complex, massive, self-interacting scalar field minimally coupled to the gravitational sector [15]. The Lagrangian governing the field dynamics reads

$$\mathcal{L}_\phi = -\frac{1}{2}g^{\mu\nu}\phi_{,\mu}^*\phi_{,\nu} - \frac{1}{2}V(|\phi|^2), \quad (3)$$

where $V(|\phi|^2)$ is the scalar potential, which includes the mass term as well as self-interactions determining the object multipole moments. Varying the total action

$$\mathcal{S} = \int d^4x \sqrt{-g} \left[\frac{R}{16\pi} - \mathcal{L}_\phi \right], \quad (4)$$

we obtain the field's equations

$$G_{\mu\nu} = 8\pi T_{\mu\nu}, \quad (5a)$$

$$\frac{1}{\sqrt{-g}}(\sqrt{-g}g^{\mu\nu}\phi_{,\mu})_{,\nu} = \frac{dV}{d|\phi|^2}\phi, \quad (5b)$$

where g is the metric determinant and $T_{\mu\nu}$ is the canonical stress-energy tensor

$$T_{\mu\nu} = \frac{1}{2}(\phi_{,\mu}^*\phi_{,\nu} + \phi_{,\mu}\phi_{,\nu}^*) - \frac{1}{2}g_{\mu\nu} [g^{\alpha\beta}\phi_{,\alpha}^*\phi_{,\beta} + V(|\phi|^2)].$$

We look for stationary and axisymmetric solutions of Eqns. (5). Using the set of coordinates $x^\mu = (t, r, \theta, \varphi)$ adapted to the isometry generators $(\frac{\partial}{\partial t}, \frac{\partial}{\partial \varphi})$, the metric and the stress-energy tensor of the solutions have no explicit dependence on t and φ . Stationarity and axisymmetry require the scalar field to satisfy the ansatz

$$\phi = \phi_0(r, \theta)e^{i(s\phi - \Omega t)}, \quad (6)$$

where the *azimuthal winding number* s is an integer related to the BS total angular momentum and $\Omega > 0$ is the

field angular frequency [39]. We adopt quasi-isotropic coordinates for the metric of a stationary and axisymmetric spacetime

$$ds^2 = -e^{\gamma+\rho}dt^2 + e^{2\alpha}(dr^2 + r^2d\theta^2) + e^{\gamma-\rho}r^2\sin^2\theta(d\varphi - \omega dt)^2, \quad (7)$$

where the four metric functions $(\gamma, \rho, \alpha, \omega)$, depend on (r, θ) only. In this work we consider a specific family of *massive* BSs [12, 35], featuring repulsive quartic self-interactions,

$$V(|\phi|^2) = m^2|\phi|^2 + \frac{1}{2}\lambda|\phi|^4. \quad (8)$$

Moreover we focus on the strong coupling limit $\lambda/m^2 \gg 1$, in which the maximum mass supported by *static* configurations scales as [12]

$$M_{\max} \sim 0.06 \frac{\sqrt{\lambda\hbar}}{m_s^2} M_p^3, \quad (9)$$

where $m_s = m\hbar$ is the mass of the boson and M_p the Planck mass. Equation (9) shows that, for $\lambda \sim \mathcal{O}(\hbar^{-1})$ and m_s in the range 1–100 MeV, stellar configurations with M_{\max} in the range $10\text{--}10^5 M_\odot$ are supported. This is different from the case of *mini* BSs described by non-interacting scalars [10, 11], where the same mass range requires ultralight bosons. Moreover, large self-interactions are also expected to quench [22] the instabilities observed in numerical simulations of rotating *mini* BSs [20, 21].

A. Perfect-fluid approximation in the strong-coupling limit

In the strong coupling regime the numerical integration of the stellar equations greatly simplifies. As discussed in [12], for spherically-symmetric solutions it is possible to identify two distinct regions in the object radial domain, corresponding to different behaviours of the field's energy density. At large values of r the BS features a *tail* region where ϕ decays exponentially as $\sim e^{-\sqrt{m^2 - \Omega^2}r}/r$. At smaller r , an inner *non-tail* region sets up, where the field has significantly larger amplitude and most of the object's mass is localized. In this zone ϕ varies on a very large scale, such that one can safely assume $\phi_{,r} \simeq 0$, while in the *tail* region, although $\phi_{,r}$ is in general not negligible, the field vanishes quickly due to the exponential suppression and can be set to zero. We have numerically confirmed the validity of these assumptions, as shown in Fig. 1, which displays the radial profile of ϕ for two spherically symmetric BSs with the same frequency, built considering $\phi_{,r}^{\text{non-tail}} \sim 0$, $\phi^{\text{tail}} \sim 0$ (solid curve) and without any approximation (dashed curve).

In the spinning case, a further simplification can be made. Indeed, as noted in [35], the symmetry of the solution suggests that the field stress-energy tensor should vary on the same scale when the star is rotating or not,

such that in both cases derivatives with respect to the radial direction and the polar angle θ can be neglected in the *non-tail* region, while in general $\phi_{,\varphi} \neq 0$. Setting

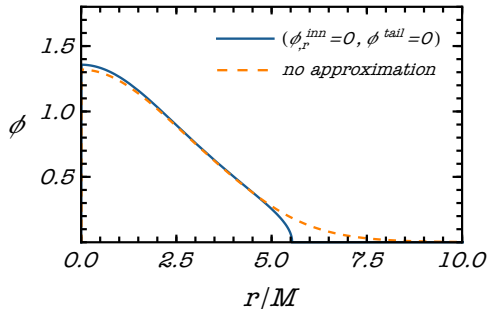


FIG. 1. Scalar field profile for a spherically-symmetric massive BS with $\lambda/m^2 = 2500$, computed (i) neglecting radial derivatives of ϕ in the inner zone, and setting $\phi = 0$ in tail zone (solid line) and (ii) with no approximations on the scalar field in the domain of integration (dashed line).

$\phi_{,r}$ and $\phi_{,\theta}$ to zero in the stress-energy tensor and using the ansatz (6), we can recast $T_{\mu\nu}$ within the inner region in the following form

$$T_{\mu\nu} = (\epsilon + P)u_\mu u_\nu + P g_{\mu\nu}, \quad (10)$$

where

$$(u_t, u_r, u_\theta, u_\varphi) = A^{-1/2}(-\Omega, 0, 0, s), \quad (11a)$$

$$A = \frac{g^{\alpha\beta} \phi_{,\alpha}^* \phi_{,\beta}}{|\phi|^2} \approx (-g^{tt} \Omega^2 + 2g^{t\varphi} \Omega s - g^{\varphi\varphi} s^2), \quad (11b)$$

and we identify the field's pressure and energy density

$$P = \frac{1}{2} A |\phi|^2 - \frac{1}{2} V(|\phi|^2), \quad (12a)$$

$$\epsilon = \frac{1}{2} A |\phi|^2 + \frac{1}{2} V(|\phi|^2). \quad (12b)$$

In the *tail* region we assume that the scalar field is negligible, and we set $T_{\mu\nu} = 0$. Therefore, within the entire domain of integration, the stress-energy tensor resembles that of a perfect fluid.

Note that, in the inner region of a rotating massive BS, the energy density develops a non-trivial topology. Indeed, neglecting the radial and polar derivatives of ϕ , the scalar field satisfies the constraint equation

$$\left(A\phi - \frac{dV}{d|\phi|^2} \phi \right) = A\phi - m^2 \phi - \lambda |\phi|^2 \phi = 0, \quad (13)$$

whose solutions are

$$\begin{cases} |\phi|^2 = \frac{A - m^2}{\lambda} & \text{if } A > m^2, \\ \phi = 0 & \text{if } A \leq m^2. \end{cases}$$

On the other hand, outside the inner region $|\phi| \sim 0$. Therefore, under the above approximations, the general expression for $|\phi|^2$ reads

$$\begin{aligned} |\phi|^2 &= \max[0, (-g^{tt} \Omega^2 + 2g^{t\varphi} \Omega s - g^{\varphi\varphi} s^2 - m^2)/\lambda] \\ &= \max \left[0, \frac{1}{\lambda} \left(\frac{(\Omega - s\omega)^2}{e^{\gamma+\rho}} - \frac{e^{\rho-\gamma} s^2}{r^2 \sin^2 \theta} - m^2 \right) \right]. \end{aligned} \quad (14)$$

The pressure, energy density, and four-velocity can be expressed in terms of $|\phi|^2$ as²

$$P = \frac{1}{4} \lambda |\phi|^4, \quad (16a)$$

$$\epsilon = m^2 |\phi|^2 + \frac{3}{4} \lambda |\phi|^4, \quad (16b)$$

$$(u_t, u_r, u_\theta, u_\varphi) = \frac{(-\Omega, 0, 0, s)}{(\lambda |\phi|^2 + m^2)^{\frac{1}{2}}}. \quad (16c)$$

By combining Eqns. (14)-(16) one can see that the energy density of rotating BSs develops a toroidal shape, as evident from Eq. (14) which shows that $|\phi|^2$ is zero near the polar axis where $\sin \theta \approx 0$. This behaviour is displayed in Fig. 2 for a representative model. Note also that, in the absence of rotation, the torus degenerates into a spherical profile.

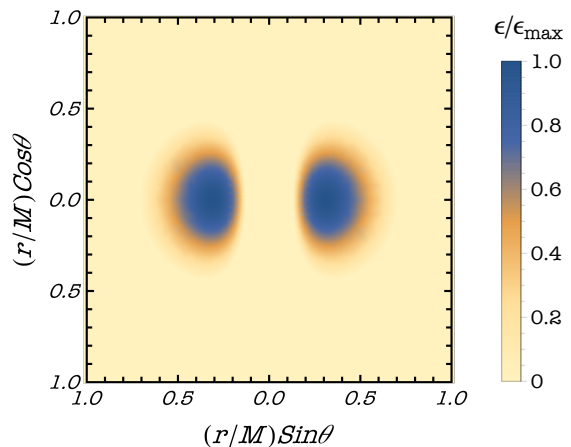


FIG. 2. Vertical cross-section of a fast rotating BS with $M = 0.04 M_B$ and $\chi = J/M^2 = 1.3$. The scalar field energy density is normalized to its maximum value.

² Therefore, in this approximation the interior of the star is described by a perfect fluid with a barotropic equation of state

$$P(\epsilon) = \frac{m^4}{\lambda} \left(1 + \sqrt{1 + \frac{3\epsilon\lambda}{m^4}} \right)^2. \quad (15)$$

B. Coordinate rescaling

Our numerical analysis can be further simplified by a suitable change of variables which removes both m and λ from the field's equations. In geometrical units $[\lambda] = [\text{mass}]^{-2}$ and $[m] = [\text{mass}]^{-1}$, such that the ratio $M_B \equiv \lambda^{\frac{1}{2}}/m^2$ has the dimension of a mass. We can then introduce the following dimensionless quantities:

$$\tilde{t} = t/M_B \quad , \quad \tilde{r} = r/M_B \quad , \quad (17a)$$

$$\tilde{P} = PM_B^2 \quad , \quad \tilde{\epsilon} = \epsilon M_B^2 \quad , \quad \tilde{\omega} = \omega M_B \quad . \quad (17b)$$

It is also convenient to define the dimensionless frequency $\tilde{\Omega} = \Omega/m \in (0, 1)$, where for a BS Ω is always smaller than m , and the limit $\tilde{\Omega} \rightarrow 1$ corresponds to the non-relativistic (weak self-gravity) regime.

We can now scale the remaining dimensionless quantities by the ratio $\lambda^{1/2}/m$, in order to factor out the coupling constant from our equations:

$$\tilde{s} = \frac{m}{\lambda^{\frac{1}{2}}} s \quad , \quad |\tilde{\phi}|^2 = \frac{\lambda}{m^2} |\phi|^2 \quad . \quad (18)$$

Physical quantities can be restored after having solved the numerical problem by multiplying the dimensionless ones by different powers of M_B to match the correct mass dimensions.

Hereafter we use \tilde{s} as an input for the numerical integration of the field equations and treat it as a continuous parameter. This is a valid approximation for configurations with large values of s since, by virtue of the first relation in Eq. (18), the magnitude of \tilde{s} will be large compared to the spacing between two consecutive values, since $m/\lambda^{1/2} \ll 1$ [35]. Solutions with a given \tilde{s} can also be regarded as configurations with small s . This, however, implies a constraint on the physical masses and spins of the dimensionful rescaled configurations, since the ratio $\lambda^{1/2}/m$ becomes necessarily a multiple of $1/\tilde{s}$. Moderate and fast spinning BSs with small s cannot be obtained with our method, because they will have large \tilde{s} and the first equation in (18) cannot be satisfied without violating the assumption $\lambda^{1/2}/m \gg 1$. Indeed BSs with small s and large χ only exist outside the strong self-coupling limit. With the variable transformations in Eqns. (17)-(18), the problem translates in solving the Einstein equations for the metric specified by the line element

$$d\tilde{s}^2 = -e^{\gamma+\rho} d\tilde{t}^2 + e^{2\alpha} (d\tilde{r}^2 + \tilde{r}^2 d\theta^2) + e^{\gamma-\rho} \tilde{r}^2 \sin^2 \theta (d\varphi - \tilde{\omega} d\tilde{t})^2 \quad , \quad (19)$$

where the dimensionless metric functions ρ, γ , and α are the same as in Eq. (7). The stress-energy tensor in dimensionless variables reads

$$\tilde{T}_{\mu\nu} = (\tilde{\epsilon} + \tilde{P}) \tilde{u}_\mu \tilde{u}_\nu + \tilde{P} \tilde{g}_{\mu\nu} \quad , \quad (20a)$$

$$(\tilde{u}_{\tilde{t}}, \tilde{u}_{\tilde{r}}, \tilde{u}_\theta, \tilde{u}_\varphi) = \frac{(-\tilde{\Omega}, 0, 0, \tilde{s})}{(|\tilde{\phi}|^2 + 1)^{\frac{1}{2}}} \quad , \quad (20b)$$

$$\tilde{\epsilon} = |\tilde{\phi}|^2 + \frac{3}{4} |\tilde{\phi}|^4 \quad , \quad \tilde{P} = \frac{1}{4} |\tilde{\phi}|^4 \quad , \quad (20c)$$

and the scalar field constraint becomes

$$|\tilde{\phi}|^2 = \max \left[0, \frac{(\tilde{\Omega} - \tilde{s}\tilde{\omega})^2}{e^{\gamma+\rho}} - \frac{e^{\rho-\gamma} \tilde{s}^2}{\tilde{r}^2 \sin^2 \theta} - 1 \right] \quad . \quad (21)$$

For the sake of clarity, unless specified differently in the text, hereafter we shall drop the tilde from rescaled variables, and we will assume that all quantities are dimensionless.

III. A SELF-CONSISTENT METHOD FOR EQUILIBRIUM CONFIGURATIONS

Finding BS solutions of the field equations (5) requires to solve an elliptic boundary value problem. To this aim we adopt the self-consistent method presented in [35], as an application of Hachisu self-consistent field approach. The essence of this method lies in turning Einstein equations into an integral form which allows for an iterative resolution scheme. The first step toward the solution is writing the field equations in order to isolate on one side all operators having known Green functions and on the other side terms which can be regarded as effective sources.

The Einstein equations for ρ, γ and ω can be written in the following form [40]:

$$\Delta(\rho e^{\frac{\gamma}{2}}) = S_\rho(r, \mu) \quad , \quad (22a)$$

$$\left(\Delta + \frac{1}{r} \frac{\partial}{\partial r} - \frac{1}{r^2} \mu \frac{\partial}{\partial \mu} \right) \gamma e^{\frac{\gamma}{2}} = S_\gamma(r, \mu) \quad , \quad (22b)$$

$$\left(\Delta + \frac{2}{r} \frac{\partial}{\partial r} - \frac{2}{r^2} \mu \frac{\partial}{\partial \mu} \right) \omega e^{\frac{\gamma-2\rho}{2}} = S_\omega(r, \mu) \quad , \quad (22c)$$

where $\mu = \cos \theta$, Δ is the Laplacian operator in spherical coordinates, and the sources appearing on the right hand side are known expressions of the metric functions and their derivatives.

The differential equation (22a) can be put in an integral form with the use of the three-dimensional Laplacian Green function:

$$\rho = -\frac{e^{-\frac{\gamma}{2}}}{4\pi} \int_0^\infty dr' \int_{-1}^1 d\mu' \int_0^{2\pi} \frac{d\varphi' r'^2}{|r-r'|} S_\rho(r', \mu') \quad . \quad (23)$$

Using the expansion of $1/|r-r'|$ in powers of r'/r (resp., r/r'), valid for $r' < r$ (resp., $r < r'$), one obtains the following integro-differential equation:

$$\rho(r, \mu) = -e^{-\gamma/2} \sum_{n=0}^{\infty} \int_0^\infty dr' R_\rho^n(r, r') \times \int_0^1 d\mu' P_{2n}(\mu) P_{2n}(\mu') S_\rho(r', \mu') \quad , \quad (24)$$

where $P_{2n}(\mu)$ are the Legendre polynomials and

$$R_\rho^n(r, r') \equiv \frac{(r')^{2n+2}}{r^{2n+1}} \Theta(r' - r) + \frac{r^{2n}}{(r')^{2n-1}} \Theta(r - r') \quad . \quad (25)$$

Analogous expressions can be found for Eqns. (22b)-(22c) with the same form as Eq. (24):

$$f_i \propto e^{\hat{v}(f)} \sum_{n=1}^{\infty} \int_0^{\infty} dr' R_{f_i}^n(r, r') \times \int_0^1 d\mu' M_{f_i}^n(\mu, \mu') S_{f_i}(r', \mu'),$$

where $f = (\rho, \gamma, \omega)$, \hat{v} is a linear function of f , $R_{\gamma}^n(r, r')$, $R_{\omega}^n(r, r')$ have the structure of Eq. (25) and $M_f^n(\mu, \mu')$ is an angular function including Legendre and associate Legendre polynomials. The asymptotic flatness conditions $\rho \sim \mathcal{O}(1/r)$, $\gamma \sim \mathcal{O}(1/r^2)$, $\omega \sim \mathcal{O}(1/r^3)$ for $r \rightarrow \infty$, are automatically satisfied if the source terms fall off sufficiently fast at large distances. We refer the reader to Appendix A for the full expression of the source terms.

Finally, the remaining metric function α can be determined by integrating the differential equation

$$\alpha_{,\mu}(r, \mu) = S_{\alpha}(r, \mu), \quad (26)$$

together with the condition that $\alpha = \frac{1}{2}(\gamma - \rho)$ at the pole, where $S_{\alpha}(r, \mu)$ is given by Eq. (A4).

IV. MULTIPOLE MOMENTS

Relativistic multipole moments characterize the structure of astrophysical compact objects, their gravitational field, including non-linear contributions [41] and their GW emission [23]. The actual computation of the multipole moments greatly simplifies in a wide class of *asymptotically Cartesian and mass centered* coordinates [42], which allows reading the multipole moments directly off the asymptotic behavior of the metric coefficients. Rotating axial (and equatorial) symmetry BSs are characterized by two families of scalar multipoles, the mass $\{M_{2i}\}_{i=0, \dots, \infty}$ and the current $\{S_{2i-1}\}_{i=1, \dots, \infty}$ moments, which can be extracted from the asymptotic behavior of the metric functions as in [35]:

$$\rho = - \sum_{n=0}^{\infty} \left[2 \frac{M_{2n}}{r^{2n+1}} + \mathcal{O}\left(\frac{1}{r^{2n+2}}\right) \right] P_{2n}(\mu), \quad (27a)$$

$$\omega = - \sum_{n=1}^{\infty} \left[\frac{2}{2n-1} \frac{S_{2n-1}}{r^{2n+1}} + \mathcal{O}\left(\frac{1}{r^{2n+2}}\right) \right] \frac{P_{2n-1}^1(\mu)}{\sin \theta}, \quad (27b)$$

with the lowest multipoles $M_0, S_1 \equiv J$, and M_2 corresponding to the mass, angular momentum, and quadrupole moment, respectively. Comparing Eqns. (27) with the explicit form of the metric in Eqns. (A1a)-(A1c) it is straightforward to identify the mass and current mo-

ments as integrals over the source terms S_{ρ} and S_{ω} :

$$M_{2n} = \frac{1}{2} \int_0^r dr' (r')^{2n+2} \int_0^1 d\mu' P_{2n}(\mu') S_{\rho}(r', \mu'), \quad (28a)$$

$$S_{2n-1} = \frac{1}{4n} \int_0^r dr' (r')^{2n+2} \times \int_0^1 d\mu' \sin \theta' P_{2n-1}^1(\mu') S_{\omega}(r', \mu'). \quad (28b)$$

However, as noticed in [43], the specific choice of radial coordinate leading to the line element (19) renders the identifications of the multipole moments with the coefficients M_{2n} and S_{2n} ambiguous. To correctly match the definition of multipole moments given by Geroch and Hansen [41], all terms in Eq. (27) with $n \geq 2$ must be corrected by adding a mass-spin dependent shift, yielding for the lowest moments:

$$M_2^{\text{GH}} = M_2 - \frac{4}{3} \left(\frac{1}{4} + \frac{\gamma_0}{M_0^2} \right) M_0^3, \quad (29a)$$

$$S_3^{\text{GH}} = S_3 - \frac{12}{5} \left(\frac{1}{4} + \frac{\gamma_0}{M_0^2} \right) S_1 M_0^2, \quad (29b)$$

where M_{2n}^{GH} and S_{2n-1}^{GH} are Geroch-Hansen moments, and the coefficient γ_0 can be read-off from the asymptotic $1/r$ expansion

$$e^{\gamma} \sim \sqrt{\frac{\pi}{2}} \left[\left(1 + \frac{\gamma_0}{r^2} \right) T_0^{1/2} + \frac{\gamma_2}{r^4} T_2^{1/2} + \dots \right], \quad (30)$$

where $T_l^{1/2}(\mu)$ are the Gegenbauer polynomials. We discuss the relevance of such corrections in Sec. VI, but we can anticipate that, for all the BS configurations that we have considered, the correction due to the shift in (29) is below 2%. For this reason, hereafter we will not distinguish between $\{M_{2n}^{\text{GH}}, S_{2n-1}^{\text{GH}}\}$ and $\{M_{2n}, S_{2n-1}\}$, discussing numerical results for the latter only.

It is convenient to introduce the *reduced* multipoles of order n :

$$\kappa_{2n} \equiv (-1)^n \frac{M_{2n}}{\chi^{2n} M_0^{2n+1}} = (-1)^n \frac{\bar{M}_{2n}}{\chi^{2n}}, \quad (31)$$

$$\sigma_{2n-1} \equiv (-1)^{n+1} \frac{S_{2n-1}}{\chi^{2n-1} M_0^{2n}} = (-1)^{n+1} \frac{\bar{S}_{2n-1}}{\chi^{2n-1}}, \quad (32)$$

with the leading multipoles being the reduced quadrupole and spin-octupole moments

$$\kappa_2 = - \frac{M_2}{\chi^2 M_0^3}, \quad \sigma_3 = - \frac{S_3}{\chi^3 M_0^4}. \quad (33)$$

These quantities are regular in the small- χ limit, and depend on the mass $M \equiv M_0$ and the effective coupling $M_B = \lambda^{\frac{1}{2}}/m^2$ only through the dimensionless combination M/M_B . For a Kerr BH, $\kappa_{2n}^{\text{BH}} = \sigma_{2n-1}^{\text{BH}} = 1$. As a comparison, for neutron stars $\kappa_2^{\text{NS}} \sim 1 \div 10$ depending on the internal composition [44, 45]. Furthermore, for a Kerr BH κ_{2n}^{BH} and $\sigma_{2n-1}^{\text{BH}}$ are independent of the spin, while for neutron stars this is true only to $\mathcal{O}(\chi^2)$.

V. NUMERICAL SCHEME

We have solved the system of equations for the metric functions and the scalar field discussed in Sec. III by using a self-consistent iterative scheme. The full solution depends on the radius and the polar angle, defined on a two-dimensional grid (r, θ) with a fixed size (see discussion in the next section). Numerical calculations have been coded in C according to the following iterative procedure:

1. We start by selecting an initial guess for the metric functions $(\rho, \gamma, \omega, \alpha)_{(1)}$, the angular frequency Ω and a specific value of s . The initial guess for the metric and the angular frequency corresponds to a solution of the field equations for a non-spinning, spherically symmetric BS as explained in Appendix B, while s is initialized to a small but non-zero value, $s \sim 0.01$.
2. From such initial configuration, we compute the energy density, pressure and scalar field amplitude $(\epsilon, P, \phi)_{(1)}$ using Eqns. (20c)-(21).
3. We replace $(\rho, \gamma, \omega, \Omega, \epsilon, P, \phi)_{(1)}$ into the source terms on the right hand side of Eqns. (A1), and perform the numerical integration, obtaining the values of the metric functions at the next step $(\rho, \gamma, \omega)_{(2)}$. The metric component $\alpha_{(2)}$ is obtained by direct integration of Eq. (26).
4. The energy density, pressure and scalar field amplitude $(P, \epsilon, \phi)_{(2)}$ are then computed from the above quantities, thus completing one full iteration of the procedure. The solution is then improved iteratively by repeating steps 1-4 until the desired convergence is reached.
5. We use weighted averages of the metric functions to boost the convergence of the algorithm. Let $f_{(k)}$ collectively represent the values of each of the four components $(\rho, \gamma, \omega, \alpha)$ after the k th iteration. Using $f_{(k)}$ to evaluate the source terms in Eq. (A1) and integrating, we obtain the new values $\tilde{f}_{(k+1)}$, which one would naively use as the inputs for the next iteration. Instead, following [40], we build the linear combinations

$$f_{(k+1)} = a\tilde{f}_{(k+1)} + (1-a)f_{(k)}, \quad (34)$$

where $a \in (0, 1)$ is a weight factor. The use of weighted averages avoids the solution to bounce among successive iterations. Hereafter we fix $a = 1/3$, which we found to provide the best compromise between the speed and the accuracy of the convergence.

6. As a convergence criterion, we ask that the maximum relative difference between the values of all

metric functions at two successive iterations, evaluated on the two-dimensional grid (r, θ) , is smaller than a threshold δ :

$$\Delta f = \max_{(r, \theta)} |f_{(i+1)}/f_{(i)} - 1| < \delta, \quad f = (\rho, \gamma, \alpha, \omega). \quad (35)$$

For example, the algorithm needs about 150 iterations for the solution to converge with a maximum relative error $\sim 10^{-5}$.

At each iteration, we adjust the input values of Ω and s in such a way that the total mass and angular momentum, as determined by Eqns. (28), are kept fixed to their predetermined desired values. This adjustment is implemented through a two-dimensional Newton-Raphson method by solving the equations $M(\Omega_k, s_k) = M_{\text{fin}}$ and $J(\Omega_k, s_k) = J_{\text{fin}}$ for (Ω_k, s_k) at each k -th iteration. This procedure allows us to choose, at the beginning of the numerical simulation, the mass and spin of the BS solution³.

The metric functions are integrated on a two dimensional discrete grid for the coordinates r and $\mu = \cos\theta$. We divide the angular domain into n_μ equally-spaced steps within $[0, 1]$. We compactify the radial direction through the change of coordinates

$$r \equiv r(q) = \frac{q}{1-q}, \quad (36)$$

such that the radial domain $r \in [0, \infty)$ is mapped into the finite domain $q \in [0, 1)$. We perform the integration between $q(r_0) = r_0/(r_0 + 1)$ and $q(r_{\text{max}}) = r_{\text{max}}/(r_{\text{max}} + 1)$, where $r_0 = 10^{-6}$ and $r_{\text{max}} = 10$, which is typically two orders of magnitude larger than the radius of the BSs considered. We have verified that our results are stable for changes of both r_0 and r_{max} . The number of grid points in the radial direction was fixed to $n_q = 600$, while in the angular domain we choose different setups depending on the spin. Small values of χ render the metric profile stiffer, and require a more refined lattice with larger values of n_μ .

Derivatives in Eqns. (A2) are numerically evaluated through a five-point central approximation, except near the inner (outer) boundary where we used forward (backward) derivatives. Integrals in Eqns. (A1) are performed using the Simpson and the trapezoidal rule for the angular and the radial domain, respectively. We checked that higher order methods for both derivatives and integrals do not lead to significant changes in our results.

Integration near the pole for Eqn. (A1a) and (A1c) is

³ Keeping M constant between different iterations is also necessary to guarantee convergence. Indeed, we found that leaving the value of Ω unchanged leads to a breakdown of the convergence after few iterations.

simplified by resorting to the angular identities

$$\lim_{\theta \rightarrow 0} \frac{\sin[(2n-1)\theta]}{(2n-1)\sin\theta} = 1, \quad (37)$$

$$\lim_{\theta \rightarrow 0} \frac{P_{2n-1}^1(\cos\theta)}{2n(2n-1)\sin\theta} = -\frac{(2n)!}{(n!)^2 2^{2n} (2n-1)}. \quad (38)$$

Finally, we fix the values of the components in the sum of Eq. (A1) to $n = 10$.

VI. RESULTS

A. Quadrupole and octupole moments of rotating massive BSs

We have studied the multipolar structure of arbitrarily rotating massive BS in the large coupling limit for different configurations specified by the spin parameter χ and by the object mass in units of M_B . To simplify the comparison with previous results in the literature, we include in our sample the range of masses considered in [35] (we refer the reader to Appendix C for further comparisons).

We have carefully investigated how the obtained solutions are sensitive to the spacing of the numerical grid. We found that self-gravitating configurations are numerically stable under changes of the radial resolution (i.e. changes in n_q), while for small spins, typically $\chi \lesssim 0.1$, the integration becomes more sensitive to the angular resolution (i.e. to changes in n_μ). At large spins $\chi \sim \mathcal{O}(1)$, the radius, frequency, and multipole moments are well determined and stable by choosing $n_q \sim n_\mu \sim \mathcal{O}(10^2)$ and setting $n = 10$ in Eq. (28a). Increasing the lattice density, as well as the cutoff value for n , typically yields changes of a few percent on the stellar structure. On the other hand, for slowly rotating BSs the calculation of multipole moments requires much larger values of $n_\mu \sim \mathcal{O}(10^4)$, to converge to a stable solution. For this reason, to extract the quadrupole and octupole moments, we set the spacing of numerical grid to $n_q \times n_\mu = 600 \times 20000$ for $\chi \leq 0.1$ and $n_q \times n_\mu = 600 \times 1000$ for $\chi \geq 0.1$.

Moreover, as already discussed in [35], we find that for $\chi = 0$ the quadrupole moment does not vanish, leading to a (small) numerical offset $M_2^{(\text{off})} = M_2(\chi = 0)$. This is a numerical artifact, as we know that $M_2 \sim \chi^2 + \mathcal{O}(\chi^4)$. Therefore, we manually subtracted the offset from the raw values, i.e., we define the physical quadrupole moments as $M_2 = M_2^{(\text{raw})} - M_2^{(\text{off})}$. The offset is negligible at large spin but it can spoil the $M_2 \sim \chi^2$ scaling at small spins. The top panels of Fig. 3 show the reduced quadrupole moment $\kappa_2^{(\text{raw})}$ as obtained from the raw value of $M_2^{(\text{raw})}$, along with the corresponding value of the offset $\kappa_2^{(\text{off})}$, as a function of n_μ for a spinning BS with $\chi = 0.1$ (left column) and $\chi = 0.0075$ (right column). The mass of both configurations is fixed to $M/M_B = 0.04$.

While, for small n_μ , $\kappa_2^{(\text{raw})}$ and $\kappa_2^{(\text{off})}$ have comparable magnitude, by increasing the value of n_μ the offset

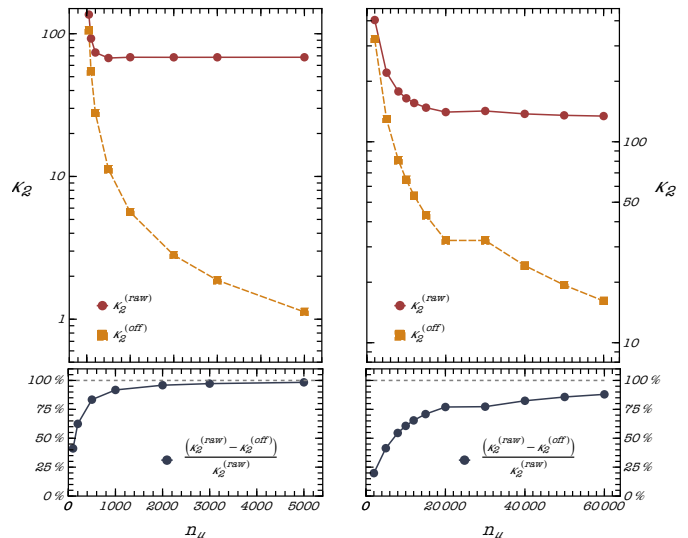


FIG. 3. (Top panels) Data points identify raw values of the reduced quadrupole moment, as well as the numerical offset, as a function of the grid angular resolution. (Bottom panels) Reduced quadrupole moment normalized by its raw value as function of the angular resolution. Left and right panels refer to BSs with spin $\chi = 0.1$ and $\chi = 0.0075$, respectively, both with $M/M_B = 0.04$.

decreases monotonically and the effect of subtracting it becomes progressively less important. This is reflected in the bottom panels of Fig. 3, where we show that $\kappa_2 / \kappa_2^{(\text{raw})} \rightarrow 1$ as the angular resolution increases. The convergence is faster for higher spins (left panel). For a low value of the spin (right panel), the offset $\kappa_2^{(\text{off})}$ contributes $\approx 25\%$ when $n_\mu = 20000$, while the contribution reduces to $\approx 12\%$ when $n_\mu = 60000$, the convergence being monotonic with n_μ . This is coherent with the fact, anticipated before, that convergence of the solution requires $n_\mu \simeq 10^3$ and $n_\mu \simeq 2 \times 10^4$ for $\chi \gtrsim 0.1$ and $\chi < 0.1$, respectively. We stress that only after subtracting the offset does M_2 scale as χ^2 at small spins.

We speculate that the convergence of κ_2 with n_μ can be traced back to the BS topology. Solutions with small spin resemble closely the nonrotating spherical configurations. But, however small be the spin, rotating BSs are toroidal and they have no continuum limit to the spherical topology of the nonrotating case (because, for a given mass and fixed coupling, χ can only assume discrete values). Configurations with spins close to the minimum value show a steep decrease of the energy density near the rotation axis, which requires a large number of angular points to be fully resolved.

The reduced quadrupole moments κ_2 for different BS configurations, as a function of the dimensionless mass parameter M/M_B and of the spin χ , are shown in Fig. 4. For small values of χ , κ_2 is nearly independent of the spin, i.e. $M_2 \propto \chi^2$, with the proportionality constant

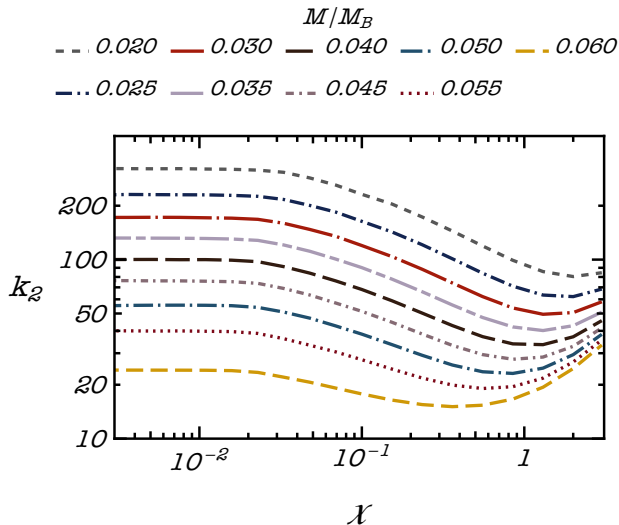


FIG. 4. Reduced quadrupole moment κ_2 as a function of the dimensionless spin χ for different values of the BS mass in units of M_B . As a comparison, $\kappa_2^{\text{BH}} = 1$ for a Kerr BH with any spin.

depending only on the object mass. In the stable branch, configurations with larger masses are also more compact. Correspondingly, for fixed spin, κ_2 decreases as the mass increases. Interestingly, κ_2 is nonmonotonic with χ , but it shows a gradual decrease between $\chi \sim 0.03$ and $\chi \sim 1$, after which it grows rapidly [35]. Note that the spin can also exceed the Kerr bound, i.e. $\chi > 1$.

The extraction of the reduced octupole moment σ_3 is more challenging due to the fact that, besides constant offsets, spurious numerical terms introduce additional nonphysical corrections at linear and quadratic order in the spin, spoiling the $\sigma_3 \sim \chi^3 + \mathcal{O}(\chi^5)$ dependence. Also in this case the offset is negligible for highly-spinning configurations.

In order to isolate the physical contribution, we fit the behavior of the octupole moment with a cubic polynomial $S_3^{(\text{raw})}(\chi) = a_0 + a_1\chi + a_2\chi^2 + a_3\chi^3$ for different small values of the spin parameter. For all BS configurations considered, we find non-zero values for the three coefficients $a_{0,1,2}$, with $a_0 \sim a_2 \ll a_1$. After subtracting the constant, linear, and quadratic terms from the raw octupole moments, we recover the correct dependence $S_3 \sim \chi^3$. Furthermore, to reduce the numerical noise, which can potentially affect the precision of the fit, we averaged over the last 50 iterations of the algorithm, where Δf in Eq. (35) oscillates about its minimum value. As for M_2 , we find that the spurious coefficients $a_{0,1,2}$ decrease for higher angular resolution (i.e., for larger values of n_μ).

However, the extraction of σ_3 is problematic for masses close to $M/M_B \simeq 0.06$, i.e., to the maximum mass of non rotating BSs. As already observed in [35], the octupole moment is small for such masses and its accurate determination is prevented by numerical uncertainties. For this

reason, we do not report the corresponding data. For the other configurations analyzed in Fig. 4, the reduced spin-octupole moment $\sigma_3 = -S_3/\chi^3 M^4$, obtained through the procedure described above, is shown in Fig. 5. As for the

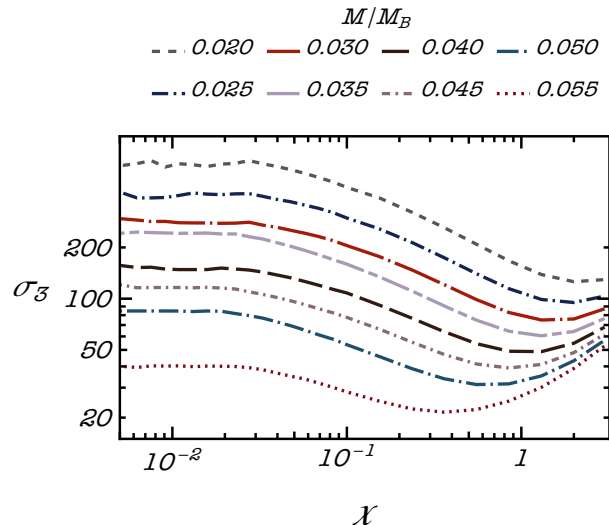


FIG. 5. Reduced spin-octupole moment σ_3 as a function of the dimensionless spin χ for the same BS masses of Fig. 4. As a comparison, $\sigma_3^{\text{BH}} = 1$ for a Kerr BH with any spin.

quadrupole moments, the curves are constant at small spins and exhibit a transition to a region with negative slope in correspondence roughly of the same values of χ .

The data for the quadrupole and octupole as a function of the spin χ and mass M/M_B are publicly available online [46].

The values for κ_2 and σ_3 plotted above ignore the corrections in the definition of the Geroch-Hansen multipole moments, Eq. (29). We show that, indeed, these corrections introduce a shift at the (sub-)percent level and therefore they can be ignored at the current numerical precision. As a representative example, we focus on a specific BS configuration with mass $M = 0.06M_B$ and different values of the spin. The corrections to the reduced quadrupole are shown in the last column of Table I for such models. We find that corrections to κ_2 are in general small, never exceeding a relative difference $\sim 2\%$, for the whole range of spins considered. The correction is larger for more compact configurations, therefore, given that $M = 0.06M_B$ corresponds to the maximum value of the compactness for non-spinning BSs, changes in κ_2 are even smaller for lower values of the mass, as those analysed in Fig 4. This picture holds as well for σ_3 , for which we find corrections smaller than 0.6% for configurations near the maximum considered mass.

Finally, we have also checked that the first moments, namely the mass and spin as computed from Eqs. (27)

χ	κ_2	κ_2^{new}	correction[%]
0.1	22.4	22.1	-1.4%
0.2	15.7	15.6	-0.5%
0.5	15.2	15.3	$\gtrsim +0.1\%$
0.8	16.4	16.4	$\gtrsim +0.1\%$
1.0	17.4	17.5	$\gtrsim +0.1\%$
1.3	19.3	19.4	$\gtrsim +0.1\%$
2.0	24.6	24.6	$\gtrsim +0.05\%$

TABLE I. Corrections to the reduced quadrupole moment derived in [43], for different value of the spin χ and $M = 0.06M_B$.

agree with those obtained from the Komar integrals [47]:

$$M = -8\pi \int_0^\infty dr \int_0^1 d\cos\theta r^2 e^{2\alpha+\gamma} \left(T_t^t t^t - \frac{1}{2} T^t t \right),$$

$$J = 4\pi \int_0^\infty dr \int_0^1 d\cos\theta r^2 e^{2\alpha+\gamma} T_\varphi^t.$$

B. Maximum mass, compactness, ergoregions

Together with the multipolar structure, our framework allows describing various features of rotating BSs, such as the dependence of the maximum mass and of the compactness on the spin and frequency, as well as the presence of ergoregions.

Due to centrifugal forces which work against the gravitational collapse, rotating BSs can support larger masses, compared to their spherically symmetric counterparts, as also shown by the mass-frequency curves in Fig. 6 for four representative families of solutions with different value of \tilde{s} ⁴.

For a given value of \tilde{s} the mass of each sequence of solutions grows as Ω decreases, until the maximum mass is reached, which is identified in our code by a failure of the algorithm to converge. Previous studies, which focused on massive BSs with non-rescaled winding number $s = 1$, showed that such sequences are continuously connected for smaller frequencies to linearly unstable branches, in which $dM/d\Omega < 0$ [48].

Figure 6 also shows the values of χ for the different configurations. Families of solutions with large \tilde{s} have high spins as long as their frequency remains large. In particular, note that also configurations with $\chi \gg 1$ are allowed. As Ω decreases along the curve, the mass and compactness increase and χ rapidly falls, approaching a

⁴ As explained in Sec. V our code uses χ as input parameter. However, for the maximum mass analysis, we have changed the workflow in order to have \tilde{s} , together with the BS mass, as input. We also remark that, as discussed in Sec. II B, the rescaled winding number \tilde{s} does not need to be an integer and it depends on the coupling constants λ and m as in Eq. (18).

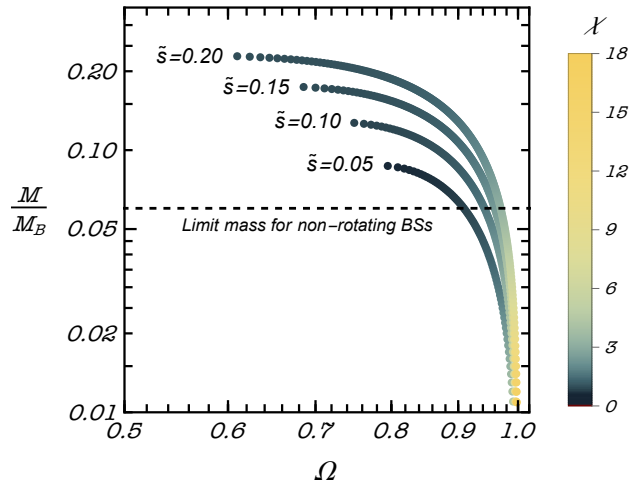


FIG. 6. Boson star mass as a function of the frequency Ω for four different values of \tilde{s} . The color range of each configurations is mapped to the value of the χ , with, darker (lighter) tones corresponding to smaller (larger) spins.

value $\chi(M_{\text{max}}) < 1$. Moreover, $\chi(M_{\text{max}}) \simeq 1$ for all stars with \tilde{s} large enough that significative rotation rate and compactnesses are approached along the curve.

Beside the maximum mass, we have also analysed the dependence on Ω of the BS compactness $\mathcal{C} = M/R$, with

$$R = R_0 e^{\rho(R_0, \pi/2) - \gamma(R_0, \pi/2)},$$

being the perimetral radius and R_0 the stellar radius, i.e. the value of the r -coordinate for which the scalar field vanishes, marking the division between the tail and the non-tail region (see Sec. II A). Figure 7 shows \mathcal{C} as a function of the frequency, for the same stellar configurations considered before, plus other five with larger \tilde{s} .

Interestingly, for $\tilde{s} \lesssim 0.2$, the compactness depends linearly on the frequency and the relation is independent of the value of \tilde{s} (or χ). The latter only affects the minimum value of the frequency which can be reached by each family and the mass profile. This linear relation holds also for mini BSs in the stable branch, as can be appreciated examining the data in [49].

All families with $\tilde{s} \gtrsim 0.25$ reach a maximum value $\mathcal{C}_{\text{max}} \simeq 0.4$, smaller than the Buchdahl limit⁵, around $\Omega_{\text{min}} \simeq 0.5$.

Due to their large compactness, it is reasonable to expect that massive and fast spinning configurations develop ergoregions. Figure 8 shows indeed a sequence of BSs at the maximum mass allowed for a given value of χ , which feature an ergoregion for sufficiently high spin.

⁵ Note that although massive BSs in the strong coupling limit are described by a perfect fluid stress energy tensor, the Buchdahl limit [50] does not apply due to rotation [2].

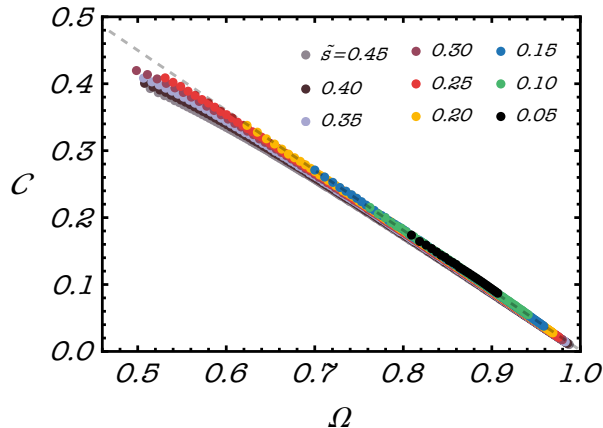


FIG. 7. Colored dots identify the BS compactness as a function of the frequency for stars with \tilde{s} in the range (0.05, 0.45). The mass for each family, varies between $M = 0.06M_B$ and the maximum mass allowed by \tilde{s} . The dashed black line corresponds to a linear fit of the data for $\tilde{s} \leq 0.2$, i.e. $C = 0.9(1 - \Omega)$.

Notice that the first appearance of an ergoregion is for a configuration with $\chi \gtrsim 0.9$, $C \gtrsim 0.30$. Such a BS has $\tilde{s} \sim 0.1$, which translates, in the $\lambda^{1/2}/m \gg 1$ limit, to a winding number $s \gg 1$. The ergoregion shown in Fig. 8 arise for solutions in the stable branch⁶. However, although stable against radial perturbations, BSs with an ergoregion are unstable over longer timescales against nonspherical modes due to the so-called ergoregion instability [51, 52]. An interesting followup of our work could be to quantify the instability time scale for our configurations.

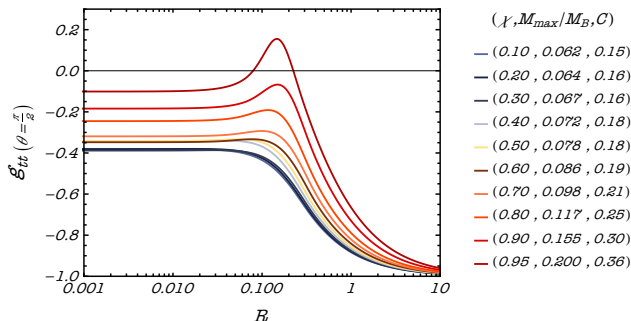


FIG. 8. Metric component g_{tt} as function of the radius on the equatorial plane, for configurations corresponding to the maximum mass at a given spin χ . For $(\chi, M) = (0.95, 0.2M_B)$ the g_{tt} changes sign twice, revealing the presence of an ergoregion with toroidal topology.

⁶ This is different from the case of mini BSs, which exhibit ergoregions only for configurations in the unstable branch [49].

VII. CONCLUSIONS AND DISCUSSION

In this work we constructed fully relativistic solutions of rotating BSs with quartic self-interactions within a perfect fluid approximation scheme, valid in the large self-coupling regime. The Einstein equations have been solved with a numerical C code implementing the iterative method described in [35], which allows us to find configurations covering a wide portion of the parameter space, including those which are more relevant for phenomenology. Indeed, since the coupling constants are completely factored out from the numerical solution, each configuration corresponds to a family of BSs, sharing the same compactness and dimensionless spin but differing in the mass, the latter scaling linearly with the combination of the self-coupling and the boson's mass defined in Sec. II B.

We characterized the multipolar structure of these BSs up to the spin-octupole contribution, considering different sequences of compact configurations with constant mass, spanning a two-dimensional region in the mass-spin parameter space, including the slowly rotating regime. The values of the quadrupole and spin-octupole moments have been computed significantly more accurately than in previous work.

Our results, summarized in Fig. 4 and Fig. 5, confirm that the quadrupole moment is proportional to χ^2 (as in the Kerr case) but only for slowly spinning BSs and that the constant reduced quadrupole moment in that regime has a minimum, causing the range of values of κ_2 to be not continuously connected to the BH value $\kappa_2^{\text{BH}} = 1$. We found such minimum, as well as the reduced multipoles, except for very large spin configurations, to be larger than what reported in previous work. We also confirmed that the spin-octupole is proportional to χ^3 (as in the Kerr case) only for low spins.

Moreover, we discussed the masses and compactness of these objects, analyzing solutions with fixed rescaled winding number \tilde{s} and for given values of the coupling constants. We showed that the maximum BS mass increases considerably for high \tilde{s} and, as it grows, the maximum mass configuration is reached for lower and lower frequencies. The corresponding compactnesses approaches $C \sim 0.4$, while the dimensionless spin parameter χ is close to unity. We found that some of these configurations have ergoregions in the branch connected to the Newtonian limit $\Omega \rightarrow 1$.

Among various theoretical and observational applications of our results, multipole moments have interesting phenomenological consequences related to the so-called universal relations [45]. Indeed, it is known that approximated analytical relations exist between certain observables of a neutron star, such as the spin-induced quadrupole moment, the tidal deformability Λ , and the moment of inertia, which are roughly insensitive of the underlying equation of state [53]. The same functional form of these relations holds also for the reduced quadrupole moment of slowly spinning massive BSs and

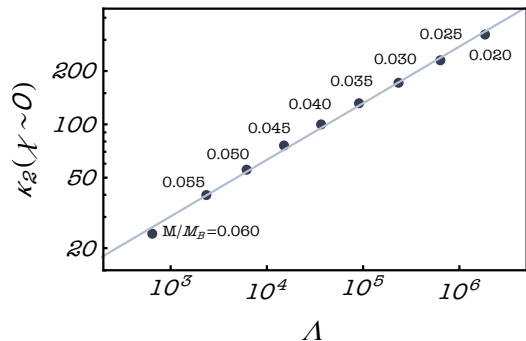


FIG. 9. Reduced quadrupole moment κ_2 as a function of the tidal deformability for different values of the BS mass, in the low spin region, $\chi \lesssim 0.02$.

its corresponding Λ , as we have recently shown [6]. The numerical calculations discussed in this paper allows to strengthen our previous result, obtained with limited data and accuracy. Using the fits for Λ provided in Ref. [54], the $\kappa_2 - \Lambda$ relation is shown Fig. 9, with the straight line identifying the semi-analytical fit

$$\log \kappa_2 \simeq 1.2 + 0.32 \log \Lambda. \quad (39)$$

We measured the distance of the data from the fit as the root mean square relative error $\sigma_E = 0.01$, where $\sigma_E^2 = \frac{1}{N} \sum_{n=1}^N (r_E^i)^2$ and $r_E^i = \kappa_2^i - (1.2 + 0.32\Lambda^i)$ are the residuals.

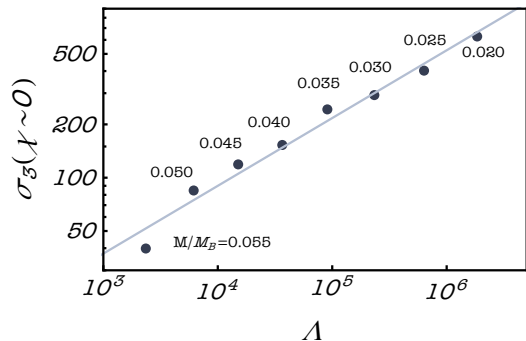


FIG. 10. Reduced spin-octupole moment σ_3 as a function of the tidal deformability for different values of the BS mass, in the low spin region, $\chi \lesssim 0.02$. As for the quadrupole in Fig. 9, we show the best-fit line, corresponding to $\sigma_3 \simeq 0.98 + 0.38 \log \Lambda$. The distance from the fit is measured by $\sigma_E = 0.03$.

We also used the data in Fig. 5 to explore the $\sigma_3 - \Lambda$ relation. To reduce the numerical noise of σ_3 at low spins, we average $\sigma_3(\chi \sim 0)$ over 10 points for $\chi \lesssim 0.02$, for each value of the mass. The data are shown in Fig. 10 and suggest that a simple linear relation exists as well between $\log \kappa_2$ and $\log \Lambda$. The relations discussed above might have many applications and are especially useful to break degeneracies among parameters that characterise gravitational waveforms [6]. On the theoretical side, proving that such $\kappa_2 - \Lambda$ and $\sigma_3 - \Lambda$ relations also exist for other scalar field interactions is an interesting and challenging task, which will shed light on the origin of the universality, and will be investigated in a followup publication. The results presented in this work are valid as long as the self-coupling is large, in which case the anisotropies of the star are negligible. Nonetheless the approach is not limited to BSs with $s \gg 1$, even if, for small s , only slowly rotating configurations can fully satisfy the requirement $\lambda/m^2 \gg 1$ coherently with the first of Eqs. (18). The extension of these results to the generic coupling regime and to different BSs potentials will be explored elsewhere. Likewise, it would be interesting to extend our analysis to compute the multipolar structure of Proca stars [13] or of Kerr BHs with bosonic hair [55–58].

ACKNOWLEDGMENTS

We are indebted to Carlos Herdeiro for discussions and comments on the manuscript. Numerical calculations have been made possible through a CINECA-INFN agreement, providing access to resources on MARCONI at CINECA. We acknowledge financial support provided under the European Union’s H2020 ERC, Starting Grant agreement no. DarkGRA–757480. We also acknowledge support under the MIUR PRIN and FARE programmes (GW-NEXT, CUP: B84I20000100001), and from the Amaldi Research Center funded by the MIUR program “Dipartimento di Eccellenza” (CUP: B81I18001170001).

Appendix A: Field equations for arbitrarily spinning BSs in the large coupling limit

In this Appendix we provide the full integral form of the equations for the metric functions ρ, γ and ω , derived in [40]:

$$\rho(r, \mu) = -e^{-\gamma/2} \sum_{n=0}^{\infty} P_{2n}(\mu) \left[\frac{1}{r^{2n+1}} \int_0^r dr' (r')^{2n+2} \int_0^1 d\mu' P_{2n}(\mu') S_\rho(r', \mu') \right. \\ \left. + r^{2n} \int_r^\infty dr' \frac{1}{(r')^{2n-1}} \int_0^1 d\mu' P_{2n}(\mu') S_\rho(r', \mu') \right], \quad (\text{A1a})$$

$$\gamma(r, \mu) = -\frac{2}{\pi} e^{-\gamma/2} \sum_{n=1}^{\infty} \frac{\sin[(2n-1)\theta]}{(2n-1)\sin\theta} \left[\frac{1}{r^{2n}} \int_0^r dr' (r')^{2n+1} \int_0^1 d\mu' \sin[(2n-1)\theta'] S_\gamma(r', \mu') \right. \\ \left. + r^{2n-2} \int_r^\infty dr' \frac{1}{(r')^{2n-3}} \int_0^1 d\mu' \sin[(2n-1)\theta'] S_\gamma(r', \mu') \right], \quad (\text{A1b})$$

$$\omega(r, \mu) = -e^{\rho-\gamma/2} \sum_{n=1}^{\infty} \frac{P_{2n-1}^1(\mu)}{2n(2n-1)\sin\theta} \left[\frac{1}{r^{2n+1}} \int_0^r dr' (r')^{2n+2} \int_0^1 d\mu' \sin\theta' P_{2n-1}^1(\mu') S_\omega(r', \mu') \right. \\ \left. + r^{2n-2} \int_r^\infty dr' \frac{1}{(r')^{2n-3}} \int_0^1 d\mu' \sin\theta' P_{2n-1}^1(\mu') S_\omega(r', \mu') \right]. \quad (\text{A1c})$$

The functions $P_n(\mu)$ and $P_n^m(\mu)$ correspond to the Leg-

endre and associate Legendre polynomials, respectively. The sources, defined in Eqns. (22a)-(22c), read

$$S_\rho(r, \mu) = e^{\gamma/2} \left\{ 8\pi e^{2\alpha} (\epsilon + P) \frac{1+v^2}{1-v^2} + r^2(1-\mu^2)e^{-2\rho} \left(\omega_{,r}^2 + \frac{1-\mu^2}{r^2} \omega_{,\mu}^2 \right) + \frac{1}{r} \gamma_{,r} - \frac{\mu}{r^2} \gamma_{,\mu} \right. \\ \left. + \frac{1}{2} \rho \left[16\pi e^{2\alpha} P - \gamma_{,r} \left(\frac{1}{2} \gamma_{,r} + \frac{1}{r} \right) - \frac{1}{r^2} \gamma_{,\mu} \left(\frac{1-\mu^2}{2} \gamma_{,\mu} - \mu \right) \right] \right\}, \quad (\text{A2a})$$

$$S_\gamma(r, \mu) = e^{\gamma/2} \left[16\pi e^{2\alpha} P + \frac{\gamma}{2} \left(16\pi e^{2\alpha} P - \frac{1}{2} \gamma_{,r}^2 - \frac{1-\mu^2}{2r^2} \gamma_{,\mu}^2 \right) \right], \quad (\text{A2b})$$

$$S_\omega(r, \mu) = e^{\gamma/2-\rho} \left\{ -16\pi e^{2\alpha+\rho} \frac{v(\epsilon+P)}{(1-v^2)r\sin\theta} + \omega \left[-8\pi e^{2\alpha} \frac{(1+v^2)\epsilon+2v^2P}{1-v^2} - \frac{1}{r} (2\rho_{,r} + \frac{1}{2}\gamma_{,r}) \right. \right. \\ \left. \left. + \frac{\mu}{r^2} (2\rho_{,\mu} + \frac{1}{2}\gamma_{,\mu}) + \rho_{,r}^2 - \frac{1}{4}\gamma_{,r}^2 + \frac{1-\mu^2}{r^2} (\rho_{,\mu}^2 - \frac{1}{4}\gamma_{,\mu}^2) - r^2(1-\mu^2)e^{-2\rho} \left(\omega_{,r}^2 + \frac{1-\mu^2}{r^2} \omega_{,\mu}^2 \right) \right] \right\}. \quad (\text{A2c})$$

The parameter v entering in the previous expressions can be identified as the proper velocity with respect to the

zero angular momentum observer and is given by:

$$v = \frac{s}{\Omega - s\omega} \frac{e^\rho}{r \sin\theta}. \quad (\text{A3})$$

Finally, the function α can be determined by solving

$$\begin{aligned}
\alpha_{,\mu} = & -\frac{1}{2}(\rho_{,\mu} + \gamma_{,\mu}) + \left\{ \frac{1}{2}[r^2(\gamma_{,rr} + \gamma_{,r}^2) - (1 - \mu^2)(\gamma_{,\mu\mu} + \gamma_{,\mu}^2)] \right. \\
& \left. + r\gamma_{,r} \left[\frac{1}{2}\mu + \mu r\gamma_{,r} + \frac{1}{2}(1 - \mu^2)\gamma_{,\mu} \right] + \frac{3}{2}\gamma_{,\mu}[-\mu^2 + \mu(1 - \mu^2)\gamma_{,\mu}] \right. \\
& - r(1 + r\gamma_{,r})(1 - \mu^2)(\gamma_{,r\mu} + \gamma_{,r}\gamma_{,\mu}) - \frac{1}{4}\mu r^2(\rho_{,r} + \gamma_{,r})^2 - \frac{1}{2}r(1 + r\gamma_{,r})(1 - \mu^2)(\rho_{,r} + \gamma_{,r})(\rho_{,\mu} + \gamma_{,\mu}) \\
& \left. + \frac{1}{4}\mu(1 - \mu^2)(\rho_{,\mu} + \gamma_{,\mu})^2 + \frac{1}{4}r^2\mu(1 - \mu^2)\gamma_{,\mu}[r^2(\rho_{,r} + \gamma_{,r})^2 - (1 - \mu^2)(\rho_{,\mu} + \gamma_{,\mu})^2] \right. \\
& \left. + (1 - \mu^2)e^{-2\rho} \left(\frac{1}{4}r^4\mu\omega_{,r}^2 + \frac{1}{2}r^3(1 - \mu^2)\omega_{,r}\omega_{,\mu} - \frac{1}{4}r^2\mu(1 - \mu^2)\omega_{,\mu}^2 + \frac{1}{2}r^4(1 - \mu^2)\gamma_{,r}\omega_{,r}\omega_{,\mu} \right. \right. \\
& \left. \left. - \frac{1}{4}r^2(1 - \mu^2)\gamma_{,\mu}[r^2\omega_{,r}^2 - (1 - \mu^2)\omega_{,\mu}^2] \right) \right\} / \left\{ (1 - \mu^2)(1 + r\gamma_{,r})^2 + [\mu - (1 - \mu^2)\gamma_{,\mu}]^2 \right\}. \quad (\text{A4})
\end{aligned}$$

with appropriate boundary conditions, which correspond to (26) with $S_\alpha(r, \mu)$ written explicitly on the right hand side.

Appendix B: Initial data for rotating configurations

The self-consistent iterative scheme to build spinning BS solutions requires an initial guess for the metric functions $(\rho, \gamma, \omega, \alpha)$ and the frequency Ω . For such initial data, we choose a solution describing a nonrotating BS with the same mass of the rotating configuration we want to obtain.

In the non-spinning limit, $\tilde{\omega} \rightarrow 0$, $e^{\gamma-\rho} = e^{2\alpha}$ and the metric reduces to

$$d\tilde{s}^2 = -e^{2(\rho+\alpha)}d\tilde{t}^2 + e^{2\alpha}(d\tilde{r}^2 + \tilde{r}^2 d\theta^2 + \tilde{r}^2 \sin^2\theta d\phi^2), \quad (\text{B1})$$

in which the metric functions ρ and α are independent of the angular variable $\mu = \cos\theta$. However, for spherically symmetric solutions, it proves useful to use a metric ansatz expressed in Schwarzschild-like coordinates:

$$ds^2 = -e^{v(r)}dt^2 + e^{u(r)}dr^2 + r^2d\theta^2 + r^2\sin^2\theta d\phi^2. \quad (\text{B2})$$

A relation between the metric functions (ρ, γ, α) and (u, v) can be found once we determine a coordinate transformation that maps metric (B2) into Eq. (B1). Let's start observing that assuming $\tilde{t} = t$ we have $\rho(\tilde{r}) + \alpha(\tilde{r}) = v(r)/2$. Moreover, from the spatial components of the metric:

$$\frac{d\tilde{r}}{r} = \frac{e^{\frac{u(r)}{2}}}{r} dr, \quad (\text{B3})$$

which integrated, gives the desired map

$$\tilde{r}(r) \propto \exp\left[\int_{r_0}^r \frac{e^{\frac{u(r')}{2}}}{r'} dr'\right]. \quad (\text{B4})$$

The proportionality constant has to be fixed by requiring that $\tilde{r}(r) \rightarrow r$ when $r \rightarrow \infty$. Summarizing, the mapping

between the metric functions in the line elements (B1) and (B2) is given by

$$\begin{aligned}
\alpha(\tilde{r}) &= \log\left(\frac{r(\tilde{r})}{\tilde{r}}\right), \\
\gamma(\tilde{r}) &= \rho(\tilde{r}) + 2\alpha(\tilde{r}), \\
\rho(\tilde{r}) &= \frac{1}{2}v(r(\tilde{r})) - \alpha(\tilde{r}). \quad (\text{B5})
\end{aligned}$$

Appendix C: Comparison with previous results

We have tested the validity of our approach by comparing the numerical values obtained for the multipole moments of rotating BS, with previous results known in literature.

The left panel of Fig. 11 shows the reduced quadrupole moment κ_2 computed with our code, for five BS families with different masses, as a function of the spin χ , compared against the values obtained in [35]. Each point represents a different BS solution derived by solving field's equation on a grid $n_q \times n_\mu = 1600 \times 160$, which is the same adopted in [35]. Dashed lines correspond to data extracted from Fig. 4 of [35]. The values of the reduced quadrupole agree remarkably well on a wide range of spins, with an average relative discrepancy smaller than 7% for all the considered BS masses.

However, as discussed in Sec. V-VI, calculations of the multipole moments are sensitive to the choice of the angular spacing n_μ for small values of the spin. By increasing n_μ we find indeed that the values of κ_2 (and σ_3) start deviating from those obtained in [35].

In the right panel of Fig. 11 we show the reduced quadrupole computed using a $n_q \times n_\mu = 1600 \times 20000$ grid, again compared with data produced in [35]. While at high spins, the agreement between the two sets of results still hold, for rotating BSs with $\chi \lesssim 0.1$ our values are in general larger by a factor ~ 2 than those calculated by Ryan. We also note that for $M = 0.06M_B$, the reduced quadrupole obtained with increased accuracy features an overall change in the behavior of κ_2 as a function of χ . As explained in Sec. VI we have checked that our results saturate for large enough n_μ . Indeed, doubling

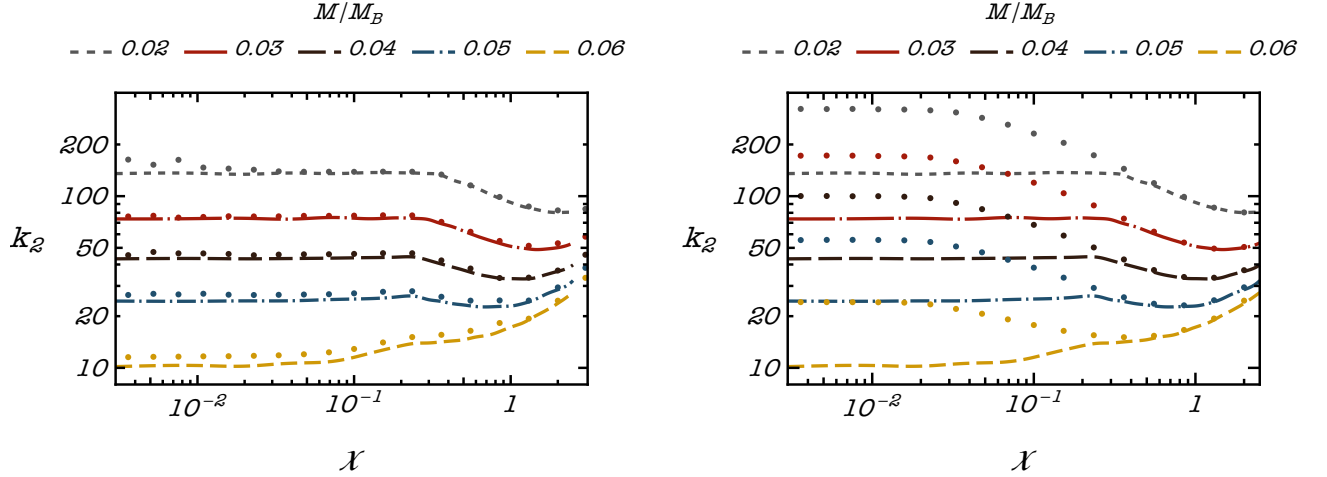


FIG. 11. Left: Reduced quadrupole moment κ_2 as a function of the dimensionless spin χ . Data points correspond to results obtained in this work setting the grid for the numerical integration of the field's equation to $n_q \times n_\mu = 1600 \times 160$. Dashed curves refer to fit of data computed with the same set up in [35]. Right: same as the left panel but with higher angular resolution, $n_q \times n_\mu = 1600 \times 20000$. The low spin constant value is a factor of ~ 2 larger than in [35] (dashed lines), while there is a very good agreement for $\chi \gtrsim 0.3$.

the grid resolution from $n_\mu = 20000$ to $n_\mu = 40000$ leads

to variation in the multipole moments smaller than 5% for $\chi \lesssim 0.1$ and even less for larger spins.

-
- [1] L. Barack *et al.*, *Class. Quant. Grav.* **36**, 143001 (2019), [arXiv:1806.05195 \[gr-qc\]](#).
- [2] V. Cardoso and P. Pani, *Living Rev. Rel.* **22**, 4 (2019), [arXiv:1904.05363 \[gr-qc\]](#).
- [3] R. Abbott *et al.* (LIGO Scientific, VIRGO, KAGRA), (2021), [arXiv:2112.06861 \[gr-qc\]](#).
- [4] E. Maggio, P. Pani, and G. Raposo, (2021), [arXiv:2105.06410 \[gr-qc\]](#).
- [5] G. F. Giudice, M. McCullough, and A. Urbano, *JCAP* **10**, 001, [arXiv:1605.01209 \[hep-ph\]](#).
- [6] C. Pacilio, M. Vaglio, A. Maselli, and P. Pani, *Physical Review D* **102**, 083002 (2020).
- [7] J. C. Bustillo, N. Sanchis-Gual, A. Torres-Forné, J. A. Font, A. Vajpeyi, R. Smith, C. Herdeiro, E. Radu, and S. H. W. Leong, *Phys. Rev. Lett.* **126**, 081101 (2021), [arXiv:2009.05376 \[gr-qc\]](#).
- [8] R. Abbott *et al.* (LIGO Scientific, Virgo), *Astrophys. J. Lett.* **900**, L13 (2020), [arXiv:2009.01190 \[astro-ph.HE\]](#).
- [9] R. Abbott *et al.* (LIGO Scientific, Virgo), *Phys. Rev. Lett.* **125**, 101102 (2020), [arXiv:2009.01075 \[gr-qc\]](#).
- [10] D. J. Kaup, *Phys. Rev.* **172**, 1331 (1968).
- [11] R. Ruffini and S. Bonazzola, *Phys. Rev.* **187**, 1767 (1969).
- [12] M. Colpi, S. L. Shapiro, and I. Wasserman, *Physical Review Letters* **57**, 2485 (1986).
- [13] R. Brito, V. Cardoso, C. A. R. Herdeiro, and E. Radu, *Phys. Lett. B* **752**, 291 (2016), [arXiv:1508.05395 \[gr-qc\]](#).
- [14] P. Jetzer, *Phys. Rept.* **220**, 163 (1992).
- [15] S. L. Liebling and C. Palenzuela, *Living Reviews in Relativity* **20**, 5 (2017).
- [16] C. Palenzuela, L. Lehner, and S. L. Liebling, *Phys. Rev. D* **77**, 044036 (2008), [arXiv:0706.2435 \[gr-qc\]](#).
- [17] C. Palenzuela, P. Pani, M. Bezares, V. Cardoso, L. Lehner, and S. Liebling, *Phys. Rev. D* **96**, 104058 (2017), [arXiv:1710.09432 \[gr-qc\]](#).
- [18] M. Bezares and C. Palenzuela, *Class. Quant. Grav.* **35**, 234002 (2018), [arXiv:1808.10732 \[gr-qc\]](#).
- [19] M. Bezares, M. Bošković, S. Liebling, C. Palenzuela, P. Pani, and E. Barausse, (2022), [arXiv:2201.06113 \[gr-qc\]](#).
- [20] N. Sanchis-Gual, F. Di Giovanni, M. Zilhão, C. Herdeiro, P. Cerdá-Durán, J. A. Font, and E. Radu, *Phys. Rev. Lett.* **123**, 221101 (2019), [arXiv:1907.12565 \[gr-qc\]](#).
- [21] F. Di Giovanni, N. Sanchis-Gual, P. Cerdá-Durán, M. Zilhão, C. Herdeiro, J. A. Font, and E. Radu, *Phys. Rev. D* **102**, 124009 (2020), [arXiv:2010.05845 \[gr-qc\]](#).
- [22] N. Siemonsen and W. E. East, *Physical Review D* **103**, 044022 (2021).
- [23] E. Poisson and C. Will, *Gravity: Newtonian, Post-Newtonian, Relativistic* (Cambridge University Press, 2014).
- [24] R. O. Hansen, *J. Math. Phys.* **15**, 46 (1974).
- [25] R. P. Geroch, *J. Math. Phys.* **11**, 2580 (1970).
- [26] M. Bianchi, D. Consoli, A. Grillo, J. F. Morales, P. Pani, and G. Raposo, *Phys. Rev. Lett.* **125**, 221601 (2020), [arXiv:2007.01743 \[hep-th\]](#).
- [27] M. Bianchi, D. Consoli, A. Grillo, J. F. Morales, P. Pani, and G. Raposo, *JHEP* **01**, 003, [arXiv:2008.01445 \[hep-th\]](#).
- [28] K. Fransen and D. R. Mayerson, (2022), [arXiv:2201.03569 \[gr-qc\]](#).
- [29] N. Loutrel, R. Brito, A. Maselli, and P. Pani, (2022), [arXiv:2203.01725 \[gr-qc\]](#).

- [30] D. Psaltis, *Living Rev. Rel.* **11**, 9 (2008), arXiv:0806.1531 [astro-ph].
- [31] J. R. Gair, M. Vallisneri, S. L. Larson, and J. G. Baker, *Living Rev. Rel.* **16**, 7 (2013), arXiv:1212.5575 [gr-qc].
- [32] N. Yunes and X. Siemens, *Living Rev. Rel.* **16**, 9 (2013), arXiv:1304.3473 [gr-qc].
- [33] E. Berti *et al.*, *Class. Quant. Grav.* **32**, 243001 (2015), arXiv:1501.07274 [gr-qc].
- [34] V. Cardoso and L. Gualtieri, *Class. Quant. Grav.* **33**, 174001 (2016), arXiv:1607.03133 [gr-qc].
- [35] F. D. Ryan, *Physical Review D* **55**, 6081 (1997).
- [36] L. Barack and C. Cutler, *Phys. Rev. D* **75**, 042003 (2007), arXiv:gr-qc/0612029.
- [37] N. V. Krishnendu, K. G. Arun, and C. K. Mishra, *Phys. Rev. Lett.* **119**, 091101 (2017), arXiv:1701.06318 [gr-qc].
- [38] N. V. Krishnendu and A. B. Yelikar, *Class. Quant. Grav.* **37**, 205019 (2020), arXiv:1904.12712 [gr-qc].
- [39] C. A. R. Herdeiro and E. Radu, *International Journal of Modern Physics D* **27**, 1843009 (2018).
- [40] H. Komatsu, Y. Eriguchi, and I. Hachisu, *Monthly Notices of the Royal Astronomical Society* **237**, 355 (1989).
- [41] R. O. Hansen, *Journal of Mathematical Physics* **15**, 46 (1974).
- [42] K. S. Thorne, *Reviews of Modern Physics* **52**, 299 (1980).
- [43] G. Pappas and T. A. Apostolatos, *Physical Review Letters* **108**, 231104 (2012).
- [44] M. Urbanec, J. C. Miller, and Z. Stuchlik, *Mon. Not. Roy. Astron. Soc.* **433**, 1903 (2013), arXiv:1301.5925 [astro-ph.SR].
- [45] K. Yagi and N. Yunes, *Phys. Rept.* **681**, 1 (2017), arXiv:1608.02582 [gr-qc].
- [46] <https://web.uniroma1.it/gmunu/>.
- [47] E. Poisson, *A Relativist's Toolkit: The Mathematics of Black-Hole Mechanics* (Cambridge University Press, Cambridge, 2004).
- [48] C. A. Herdeiro, E. Radu, and H. Rúnarsson, *Physical Review D* **92**, 084059 (2015).
- [49] J. F. Delgado, C. A. Herdeiro, and E. Radu, *Journal of Cosmology and Astroparticle Physics* **2020** (06), 037.
- [50] H. A. Buchdahl, *Phys. Rev.* **116**, 1027 (1959).
- [51] J. L. Friedman, *Communications in Mathematical Physics* **63**, 243 (1978).
- [52] V. Cardoso, P. Pani, M. Cadoni, and M. Cavaglia, *Phys. Rev. D* **77**, 124044 (2008), arXiv:0709.0532 [gr-qc].
- [53] K. Yagi and N. Yunes, *Physical Review D* **88**, 023009 (2013), arXiv: 1303.1528.
- [54] N. Sennett, T. Hinderer, J. Steinhoff, A. Buonanno, and S. Ossokine, *Phys. Rev. D* **96**, 024002 (2017), arXiv:1704.08651 [gr-qc].
- [55] C. A. R. Herdeiro and E. Radu, *Phys. Rev. Lett.* **112**, 221101 (2014).
- [56] C. A. R. Herdeiro and E. Radu, *Int. J. Mod. Phys. D* **24**, 1542014 (2015), arXiv:1504.08209 [gr-qc].
- [57] C. Herdeiro and E. Radu, *Class. Quant. Grav.* **32**, 144001 (2015), arXiv:1501.04319 [gr-qc].
- [58] C. Herdeiro, E. Radu, and H. Rúnarsson, *Class. Quant. Grav.* **33**, 154001 (2016), arXiv:1603.02687 [gr-qc].